Published in final edited form as:

Cancer Res. 2019 May 15; 79(10): 2775–2783. doi:10.1158/0008-5472.CAN-18-3565.

Molecular imaging of deoxycytidine kinase activity using deoxycytidine-enhanced CEST MRI

Zheng Han[1], **Yuguo Li**[1,2], **Jia Zhang**[1], **Jing Liu**[1,3], **Chuheng Chen**[4], **Peter C. van Zijl**[1,2], and **Guanshu Liu**[1,2,*]

[1]:Department of Radiology, Johns Hopkins University, Baltimore, MD, USA

[2]:F.M. Kirby Research Center for Functional Brain Imaging, Kennedy Krieger Institute, Baltimore, MD, USA

[3]:Radiology College, Guizhou Medical University, Guiyang, Guizhou P.R., China

[4]:Department of Biomedical Engineering, Johns Hopkins University, Baltimore, MD, USA

Abstract

Deoxycytidine kinase (DCK) is a key enzyme for the activation of a broad spectrum of nucleoside-based chemotherapy drugs (e.g., gemcitabine); low DCK activity is one of the most important causes of cancer drug-resistance. Noninvasive imaging methods that can quantify DCK activity are invaluable for assessing tumor resistance and predicting treatment efficacy. Here we developed a "natural" MRI approach to detect DCK activity using its natural substrate deoxycytidine (dC) as the imaging probe, which can be detected directly by chemical exchange saturation transfer (CEST) MRI without any synthetic labeling. CEST MRI contrast of dC and its phosphorylated form, dCTP, successfully discriminated DCK activity in two mouse leukemia cell lines with different DCK expression. This dC-enhanced CEST MRI in xenograft leukemic cancer mouse models demonstrated that DCK(+) tumors have a distinctive dynamic CEST contrast enhancement and a significantly higher CEST contrast than DCK(−) tumors ($AUC^{0-60min}$= 0.47 ± 0.25 and 0.20 ± 0.13 respectively, p=0.026, paired Student's t-test, n=4) at 1 hour after the injection of dC. dC-enhanced CEST contrast also correlated well with tumor responses to gemcitabine treatment. The present study demonstrates a novel MR molecular imaging approach for predicting cancer resistance using natural, non-radioactive, non-metallic, and clinically available agents. This method has great potential for pursuing personalized chemotherapy by stratifying patients with different DCK activity.

Introduction

The ability to stratify likely responders and non-responders through cellular and molecular determinants of responses before treatment is of paramount importance in the management of cancer chemotherapy. Among those clinically proved determinants, deoxycytidine kinase

[*]**To whom correspondence should be addressed:** Dr. Guanshu Liu, F.M.Kirby Center, Kennedy Krieger Institute, Department of Radiology, Johns Hopkins University, Office: Room 400f, Lab: Room 514, 707 N. Broadway, Baltimore MD 21205 Phone: (443)923-2751; Fax: (443)923-9505; guanshu@mri.jhu.edu.

Conflict of interests: The authors declare no potential conflicts of interest.

(DCK) is one of the essential enzymes responsible for the activation of nucleoside-based chemotherapy agents, including gemcitabine (dFdC) and cytosine arabinoside (ara-C) (1, 2). The primary role of DCK in mammalian cells is to phosphorylate 2'-deoxycytidine (dC) into deoxycytidine monophosphate (dCMP), which will be consequently converted to deoxycytidine triphosphate (dCTP) for DNA synthesis. When nucleoside-based chemotherapeutic agents enter cancer cells, they need to first be phosphorylated by DCK to transform into their active forms, which will be incorporated into DNA and abrogate DNA synthesis (3, 4). Low DCK activity has been proved to be associated with cancer resistance to dFdC and ara-C (1), with low DCK activity leading to poor survival rates in patients treated with dFdC (2). These studies suggest that DCK activity is an important biomarker for predicting cancer resistance to nucleoside analog chemotherapy agents and can be used to direct patients to the most appropriate therapy. Currently, all clinically available assays that assess tissue DCK mRNA, protein, or enzymatic activity are based on biopsy sampling (5, 6), which is prone to the risk of missing clinically relevant regions due to the limited sampling of target tissue. Thus, an imaging method that can non-invasively assess the (spatial and temporal) activity of DCK is of great clinical interest. In this context, several PET tracers have been developed (7) and very recently a patient study has been reported (8), demonstrating the promise to develop molecular imaging technologies as clinical assays for assessing DCK activity.

MRI is a versatile medical imaging modality with superb soft tissue contrast, high spatial resolution, and no ionizing radiation. It has been widely used in cancer imaging for assessing alterations at the morphological, functional, and molecular levels. In the context of enzyme detection, MRI assessments have been demonstrated for a variety of kinases using synthetic probes or genetically encoded reporters, such as creatine kinase (9), arginine kinase (10), protein kinase A (11, 12), and thymidine kinase (13). While these methods can play an important role in preclinical research, the translation of these imaging probes to human application can be formidably challenging(14). Using clinically available agents as imaging probes would be a practical strategy to overcome this challenge and allow quick translation of the preclinically validated MR molecular imaging technologies. Demonstrated in recent studies by others and us, natural biocompatible agents, such as sugars (15, 16), amino acids (17), and drugs (18, 19) can be imaged directly using a relatively new MRI contrast mechanism, chemical exchange saturation transfer (CEST) MRI, a technique that detects small amounts of contrast agent through the saturation of rapidly exchanging protons on these agents (20). Using this approach, enzyme detection has been accomplished using its natural substrates as MRI reporters (21). We hypothesized that CEST MRI can be used to detect DCK activity by intracellular conversion of its natural substrate dC and accumulation of its product dCTP, the principle of which is illustrated in Fig. 1. Our previous study (21) showed that natural dC carries exchangeable amine protons (exchange rate ~800 Hz at 37 °C and pH 7.4), enabling the direct CEST MRI detection of dC without any synthetic labeling. As depicted in Fig. 1, dC can diffuse across the cell membrane, whereas dCTP cannot. Therefore, when the cellular DCK activity is sufficiently high, the influxed dC can be quickly phosphorylated into dCTP and accumulate intracellularly. In contrast, in cells with low DCK activity, dC cannot be effectively phosphorylated and will efflux freely afterward. This thus provides a practical way to detect DCK activity in the targeted tumor cells non-

invasively through the observation of CEST MRI signal at an extended time point after the systemic administration of dC. Because dC is a clinically available agent, this “natural” MR molecular imaging method has great potential to be quickly translated to the clinic for patient stratification.

Materials and Methods

Cells

All chemicals were purchased from Sigma Aldrich (Saint Louis, MO, USA) unless otherwise stated. DCK(+) L1210-WT and DCK(−) L1210–10K murine leukemic cell lines were gift from Dr. Radu at UCLA in 2015 (7). Cells have been authenticated by short tandem repeat (STR) profiling at the Johns Hopkins Genetic Resources Core Facility (GRCF), tested to be free of mycroplasma, and used within 20 passages. The construction of these sublines of murine leukemic cancer cells was described previously (22). Cell lines have been authenticated by short tandem repeat (STR) profiling at the Johns Hopkins Genetic Resources Core Facility (GRCF) and mycoplasma contamination of cell lines were conducted 1) on establishment and characterization of a clone as a valid reagent, (2) before freezing, (3) every two months when growing in culture, (4) if the morphology or phenotypes of the cell line change unexpectedly or there is any suspicion of crosscontamination and (5) mycoplasma contamination. Cells were cultured in suspension in RPMI-1640 medium (Invitrogen, Carlsbad, CA, USA) supplemented with 10% fetal bovine serum (FBS, ThermoFisher Scientific, Waltham, MA, USA). The medium of cells were changed every two days and cells were passaged every week.

Microcapsule encapsulation

Prior to encapsulation in microcapsules, cells were incubated in culture medium containing 5 mM dC overnight. Cells were then centrifuged and washed with phosphate buffered saline (PBS, pH 7.4) three times to remove free dC. L1210-WT and L1210–10K -encapsulated microcapsules were prepared according to previously published protocols (23, 24). Microcapsules were transferred to 5 mm NMR tubes for *in vitro* MRI.

Preparation of cell extracts

Cells were incubated with 5 mM dC for 24h. After washing with PBS twice, 1×10^7 cells were pelleted and used for preparing cell extracts using the methanol–chloroform–water extraction method, an extraction method that is a widely used for high resolution NMR metabolic profiling (25, 26). Briefly, cells were suspended in 1 mL cold methanol, vortexed and added 1 mL $CHCl_3$ and 1 mL H_2O. The solution was then vigorously vortexed and kept at 4 °C overnight. The upper layer was transferred to a clean tube and methanol was evaporated by bubbling air. The remaining solution was then lyophilized and the extracts were stored at −80 °C before being suspended in 100 μL PBS (pH 7.4) for CEST MRI measurements. Lyophilized cell extracts were dissolved in deuterium oxide (D_2O) (Sigma-Aldrich, St. Louis, MO, USA) for further measurement in NMR spectrometry.

Western blot

Total cellular protein (30 g) was subjected to SDS/PAGE on 12% wt/vol acrylamide gels (Bio-Rad). Protein was transferred to nitrocellulose membrane (88018; Pierce), which was blocked overnight at 4 °C in the LiCor blocking solution (927–40000; LiCor Biosciences). Membranes were probed with primary antibodies for 1 h at room temperature. The rabbit polyclonal antibody against DCK was provided by Francoise Bontemps (University Catholique de Louvain, Belgium). The mouse anti-actin antibody (A4700; Sigma) was used as a loading control. Membranes were washed with PBST (Tween 0.1% wt/vol), probed with an infrared dye-labeled secondary antibody (926–32210 and 926–32211; LiCor Biosciences) for 1 h, washed again with PBST, and then scanned using the Odyssey infrared imaging system.

Animals

All animal experiments were performed in compliance to protocols approved by the Institutional Animal Care and Use Committee (IACUC) of Johns Hopkins University. Female NOD SCID mice (4–5 weeks, Charles River) were injected with two million tumor cells in 200 μL PBS subcutaneously into the lower flanks, with the left inoculated with L1210-WT cells and the right flank inoculated with L1210–10K cells. For dFdC treatment, mice were *i.p.* injected with 360 mg/kg dFdC suspended in saline (pH 3.3) at 7 days after inoculation. The sizes of tumors were measured from day 7 to day 11. Tumor volume (mm^3) was calculated by $width^2 \times length/2$, and tumor specific growth rates (SGR; %/day) were quantified as $\ln(volume^{day11}/volume^{day7})/5 \times 100\%$ (27). Four mice were used in each imaging group and five were used in each treatment groups.

MRI

In vitro CEST MRI was performed at 37 °C on a 9.4 T vertical bore Bruker MRI scanner using a previously reported procedure (17) with the following CEST parameters: B_1 =3.6 μT, saturation time (T_{sat})=3 sec, offsets ranging from −5 ppm to 5 ppm (step=0.2 ppm). The B_0 inhomogeneities were measured and corrected using the WASSR method (28).

At 7– 10 days after inoculation, mice were scanned using an 11.7 T Bruker Biospec horizontal scanner equipped with a mouse brain surface array RF coil (receiver) and a 72 mm volume coil (transmitter). CEST MRI was performed before and after the *i.v* injection of 200 μL dC saline solution (2 g/kg or 8.8 mmol/kg b.w.) over 30 s. A RARE-based T_2-weighted sequence was used to locate and acquire an imaging slice covering both tumors, with T_R=2 s, effective T_E=27.4 ms, RARE factor = 16, slice thickness = 1 mm, matrix size = 256 × 256, field of view=25 mm × 25 mm, number of average = 4. CEST imaging was performed using B_1=3.6 μT, T_{sat} =3 s, offsets ranging from −4 to +4 ppm (step=0.2 ppm), RARE factor =23, T_R =5 s, T_E =18.6 ms, number of averages =2, matrix size =64×64, field of view=25 mm×25 mm. The WASSR method (28) was used to assess and correct B_0 inhomogeneities. T_1 mapping was performed using a RARE-based saturation recovery sequence with six T_R times (375, 707, 1132, 1730, 2738 and 7500 ms).

Data processing

All data processing was performed using a custom program written in MATLAB (Mathworks, Waltham, MA, USA). Regions of interest (ROIs) were chosen to encompass the whole tumor based on T_2w images. Pixel-wise and average CEST spectra analyses were performed after B_0 correction using the acquired Z-spectrum. The CEST parameter $MTR_{asym}=(S^{-\Delta\omega} - S^{+\Delta\omega})/S_0$ was computed after B_0 correction and ΔMTR_{asym} at each time point calculated from MTR_{asym} (t)- MTR_{asym} (pre). MTR_{asym} maps were resized to 512×512 and denoised through wiener filtering. ΔMTR_{asym} was overlaid on the T_2w image. Area-under-curve (AUC) map was computed using the dynamic ΔMTR_{asym} in the first 60 minutes after injection according to a previously reported procedure (29). In addition, MTR_{rex} was calculated by $S_0/S^{+\Delta\omega}$ - $S_0/S^{-\Delta\omega}$. , and AREX was calculated by MTR_{rex}/T_1 (28, 30).

Immunohistofluorescence staining

Immunohistofluorescence staining was used to evaluate the expression of dCK and CD31 in L1210-WT and L1210–10K tumors. Antibodies used in this study include: mouse anti-dCK (gift from Dr. Radu (31)), rabbit mAb anti-CD31 (#77699, Cell Signal Technologies, Beverly, MA), Alexa Fluor 488-conjugated anti-rabbit IgG (#4412, Cell signaling Technologies), Alexa Fluor 594-conjugated anti-mouse IgG (#8890, Cell signaling Technologies). Tumors were embedded in optimal cutting temperature compound (OCT), frozen at −80 °C and cryosectioned at the thickness of 5 μm. Tumor sections were fixed and permeabilized using cold acetone, followed by blocking using 1% bovine serum albumin (BSA in PBS) at room temperature for 1h. Primary and secondary antibodies were applied to the tissue sequentially using recommended dilutions, with extensive washing with PBS in between. DAPI was used to stain the nucleus. Cover glass was mounted using the Prolong Antifade Mountant (Thermo Fisher Scientific). Tumor sections were imaged using a confocal laser scanning microsope (Olympus FV3000, Tokyo, Japan).

Statistical analysis

All *in vitro* experiments were performed in triplicates independently unless otherwise stated. Data are presented as mean±SEM. Two tailed Student's *t-test* was used to determine the statistical significance of the difference between groups. Differences were considered significant when $p<0.05$.

Results

CEST MRI properties of dCTP

As shown in Fig.2A, dCTP exhibits maximum CEST MRI signal (in terms of the parameter MTR_{asym}) at around 2.0 ppm, ascribed to its amine protons (18). Similar to previously reported dC data (18), the magnitude of the CEST signal of dCTP also depends on the RF saturation power (B_1) and pH (Fig. S1**)**. The minimal concentration of dCTP that can be reliably detected by CEST MRI is approximately 0.4 mM (Fig. S2**)**. While it is not possible to predict the detection threshold for all studies with different tissue properties, acquisition conditions, and saturation parameters, our study demonstrates that CEST MRI is able to

detect dCTP in a low concentration (sub-mM to mM) range even in a small volume (voxel size= $0.2\times0.2\times1$ mm^3, or 4×10^{-5} mL).

In vitro CEST detection of DCK activity in tumor cells

To demonstrate that CEST MRI can detect the accumulation of dCTP in DCK expressing cells, two leukemic cell lines, namely DCK(+) L1210-WT and DCK(−) L1210–10K (7) were used, which were encapsulated and cultured in alginate microcapsules (32) to maintain a favorable environment for the cells to survive during sample preparation and MRI scan (Fig. 2B). L1210–10K is a cell line derived by genetic mutation of the DCK gene (22). The different levels of DCK expression in those two types of cells were confirmed by western blots (Fig. 2C). Incubating with 5 mM dC for 24 hours could strongly augment the intracellular dC/dCTP concentration in the DCK (+) L1210-WT cells from 0.208 to 1.361 nmol/10^6 cells, an approximately a six-fold increase, as measured by high-resolution NMR (Fig. S3A). In contrast, the same incubation only increased the intracellular dC/dCTP concentration from 0.161 to 0.388 nmol/10^6 cells in the DCK (−) L1210–10K cells (Fig.S3B). After incubating in cell culture medium containing 5 mM dC for 12 hours and washing three times using PBS, MRI was performed. Due to their large size (diameter ~500 μm), those microcapsules could be visualized by T_2w MRI (Fig. 2D top). The CETS MRI results showed that the microcapsules containing L1210-WT cells exhibited markedly higher CEST signal at 2 ppm than those containing L1210–10K cells (Fig. 2D bottom). As shown in Fig. 2E, the mean MTR_{asym} values were 0.064± 0.014 and 0.056 ± 0.014 for L1210-WT and L1210–10K cells, respectively. Further, cell extracts from 1×10^7 L1210-WT and L1210–10K cells with or without dC incubation were prepared. A significant difference of MTR_{asym} values at 2 ppm can be observed between cell extracts of L1210-WT cells (WT) and L1210-WT cells with dC incubation (WT+dC) (p=0.0338) (Fig. 2F). In contrast, MTR_{asym} values at 2 ppm of cell extracts of L1210-WT, L1210–10K and L1210–10K were similar (p>0.05).

In vivo CEST MRI detection of DCK activity in tumors with different DCK

To demonstrate that CEST MRI can be used to detect DCK activity *in vivo*, we implanted both DCK(+) L1210-WT and DCK(−) L1210–10K cells in the flanks of mice (Fig. 3A). Immunohistochemical analyses showed no apparent differences in vessel density between the types of tumors as revealed by the CD31 staining, but a much lower DCK expression in L1210–10K tumors than in L1210-WT tumors (Fig. 3B). As illustrated in Fig. 3C, three ROIs were drawn manually for DCK (+) L1210-WT tumor, DCK(−) L1210–10K tumor and a small region of muscle. Muscle was chosen as the internal control tissue for its known low DCK activity. CEST MRI was performed before and after *i.v.* injection of 2 g/kg (8.8 mmol/kg) dC. As shown in the pre- and 60 min post-contrast MTR_{asym} maps (Fig. 3D) of a representative mouse, the DCK (+) L1210-WT tumor showed a marked CEST signal enhancement, while no apparent CEST signal increase can be observed in DCK(−) tumor and muscle. The ΔMTR_{asym} map (Fig. 3E) showed a dramatically higher ΔMTR_{asym} value in DCK (+) tumor than that in DCK (−) tumor and muscle. The averaged MTR_{asym} plots of different tumors and muscle (pre- and 1 hour post-injection) are shown in Fig. 3F, showing a noticeable increase in the CEST signal in L1210-WT tumors at around 2 ppm, but not in L1210–10K tumors and muscle (n=4).

We acquired a total of nine sets of CEST images at a temporal resolution of 7.5 minutes, which allows dynamic monitoring of the CEST signal change in each tumor over the period of 60 minutes (Fig. 4A and Fig. S4). Moreover, the two types of tumors showed distinctive dynamic contrast change in the first hour after the injection. Of note, the dynamic study showed that while the one hour post-injection time provided an optimal contrast between the two types of tumors with different DCK activity levels, any time point after 30 minutes can be potentially used. A consistent increase of MTR_{asym} is seen in DCK (+) L1210-WT tumors (ΔMTR_{asym} ~ 0.015, or 32.3 % relative CEST signal increase compared to pre-injection), while the DCK(−) L1210–10K tumor showed a strong initial increase in CEST signal (i.e., ΔMTR_{asym} =0.019 at 7.5 minutes post-injection), but a quick drop afterwards, in line with our hypothesis that DCK(+) tumors are characterized by a prolonged dC and dCTP retention (Fig. 1). We calculated the area-under-curve (AUC) maps using the CEST signal change in 0–60 min and 30–60 min after dC injection. As shown in Figs. 4B–E, the DCK (+) L1210-WT tumor showed a much stronger CEST signal ($AUC^{0–60min}$= 0.47±0.25, $AUC^{30–60min}$= 0.28±0.14, n=4) than the DCK(−) L1210–10K tumor ($AUC^{0–60min}$ =0.20±0.13, $AUC^{30–60min}$= 0.09±0.04, n=4) and muscle ($AUC^{0–60min}$=030±0.10, $AUC^{30–60min}$= 0.11±0.03, n=4) (all p values <0.05), suggesting a much stronger accumulation of dC/dCTP in the DCK(+) tumors.

Using tumors with different DCK activities to predict tumor response to gemcitabine

We first stratified the tumors based on the dC response. Comparison of the mean CEST signals before and 1 hour after the *i.v.* injection of dC (2 g/kg or 8.8 mmol/kg) showed that there was a substantial increase in CEST signal in the DCK (+) tumor, with the mean MTR_{asym} increased from 0.047±0.025 to 0.063±0.040 (p=0.0158, n=4). In contrast, no significant CEST signal change was observed in the DCK(−) tumor, with mean MTR_{asym} values of 0.055 versus 0.056 (p= 0.8622, n=4, two-tailed paired Student's t-test) (Figs. 5A and 5B). It should be noted that these changes in CEST MRI were not due to the changes in tumor T_1 relaxation times in the tumor, as the T_1-compensated analysis using the apparent exchange-dependent relaxation (AREX) approach (30) showed a similar result as that done with the MTR_{asym} approach (Fig. S5). To validate the predictive value of dC-enhanced CEST MRI, mice (n=5 in each group) bearing both L1210-WT and L1210–10K tumors were treated with either a single dose of gemcitabine (dFdC, 360 mg/kg, i.p) or vehicle (saline). Tumor sizes were measured daily after the treatment (Day 7 after inoculation) for 5 days. As shown in Fig. 5C, only the cohort of L1210-WT + dFdC showed significant decrease of tumor volume from 56.0±15.5 to 41.3±12.5 mm^3, corresponding to an −2.6% specific growth rate (SGR) per day. In contrast, the other three cohorts showed mean tumor volume increases from 67.1±26.4 to 154.8±61.9 mm^3, corresponding to a 7.3% growth rate. The mean CEST signal change (ΔMTR_{asym}) correlated negatively with tumor growth rate, indicating that higher CEST signal correlates with higher tumor response rate (Fig. 5D). Therefore, one can use the degree of CEST signal increase at 30 minutes after the dC injection to predict the chemo-resistance of a tumor to the dFdC treatment.

Discussion

Molecular imaging is expected to become an indispensable part of precision medicine by providing accurate prediction and monitoring of treatment responses (33, 34). Despite recent revolutionary developments in immunotherapy and targeted therapy, chemotherapy is still the standard of care for many types of cancers. Molecular imaging methods that can stratify patients, whose tumors will or will not respond to gemcitabine therapy, would be extremely useful. Unfortunately, no method is currently clinically available that can predict the tumor responses to gemcitabine chemotherapy, and patients are treated empirically until disease progression or worsening therapy performance. In the present study, we developed a new MR molecular imaging approach, namely dC-enhanced CEST MRI, to detect the activity of DCK, one of the key enzymes determining cancer resistance to gemcitabine. Currently, DCK activity is measurable mostly through biochemical methods (5, 6, 35), which are invasive and prone to errors stemming from limited biopsy sampling. In comparison, our approach is non-invasive, and most importantly, highly translatable as the intracellular conversion of the natural substrate dC and accumulation of its product dCTP are used to generate the MRI contrast.

Despite that a number of methods exist for imaging enzymatic activity (9–13), their clinical utility is limited due to the use of synthetic probes and genetically encoded reporters. In contrast, our approach employs only the currently used drug (nucleotide dC) and its phosphorylated product to generate MRI contrast, which can greatly reduce the translation barrier. Currently, the most widely used MRI probes are gadolinium contrast agents. However, in view of recent concerns about accumulation of gadolinium in brain and bone (36, 37), using existing nonmetallic agents and approved drugs for generating MRI contrast opens the door to the development of translatable MR molecular imaging technologies not only for enzyme activity as exemplified by the current study, but also a broad array of molecular biomarkers such as receptor ligands (38).

Our *in vitro* results showed that dC can be readily detected in the millimolar concentration range, indicative of a relatively low sensitivity. However, it should be noted that our *in vitro* experiment conditions should not be considered as the “ideal” condition to provide the optimal detectability as compared to the *in vivo* scenarios. For example, our phantom study was carried out on samples in a very small volume (~ 30 μL) at a spatial resolution of $0.2\times0.2\times1$ mm^3 (0.04 μL), which inherently has a lower signal-to-noise ratio (SNR) than a typical *in vivo* study. Strategies that can boost SNR, such as using a larger voxel size and a longer acquisition time, may improve the detectability significantly, making our method potentially applicable for clinical studies. As an analogy, ^{19}F MRSI, a method also with a typical mM concentration detection limit, has been successfully demonstrated to detect 5FU accumulated in the human tumor on a 1.5 T clinical scanner(39). Furthermore, the low sensitivity can be overcome by using highly safe agents that can be used at a high dose even in the clinical scenarios. One of such examples is glucose and its derivatives. For example, in a recent study, Rivlin *et al.* showed contrast enhanced CEST MRI using 3-O-methyl-D-glucose with a dose up to 3 g/kg (40). In the present study, we used a relatively high dose of 2 g/kg (8.8 mmol/kg). Considering the difference in the body surface area (BSA) ratio between human and mice, the human equivalent dose (HED) is approximately 13 times less

than that used in the mouse (in terms of mg/kg) (41). Hence, the dose used in our study corresponds to 153 mg/kg in the human. In fact, doses of dC have been used to antagonize the toxicity of gemcitabine and ara-C (42, 43), thymidine (44) and deoxyguanosine (45), which would be sufficient for generating detectable CEST MRI contrast. While the exact dC concentrations in the plasma or tissues were not measured in these studies, we still speculate that a mM concentration level of dCTP is achievable based on previously reported values of gemcitabine. For example, Peters et al reported that, in patients with refractory solid tumors who were infused with gemcitabine at a dose of 5700 mg/m^2 (c.a. 154 mg/kg), the peak plasma concentration of gemcitabine was measured to be as high as 512 μM and the intracellular concentration of dFdCTP (the phosphorylated form of dFdC) in the tumor cells was measured to be of 1590 pmol/10^6 cells, corresponding to 3 mM (assuming the diameter of a tumor cell is 10 μm) (46), which is in good agreement with our *in vitro* NMR spectroscopic measurement (*i.e.*, 1.361 nmol/10^6 cells). It should be noted that the calculated HED by scaling the BSA between different species is only an estimation of the safe starting dose for initial clinical studies(47) and the accurate determination of the safe dose of dC that can be used in human for an imaging purpose needs more insights into physiologic and pharmacokinetic data from animal models and humans.

It should be noted that the DCK activity is not the only reason for the dC/CTP accumulation in the tumor cells and the increase in CEST contrast. In fact, pharmacokinetics has to be taken into account as it determines how many dC molecules can be effectively delivered to the tumor. In our study, we used a dynamic imaging scheme to show that both types of tumors have similar initial uptake of dC, indicating the difference in tumor contrast was not caused by a difference in vascular permeability and perfusion. DCE-MRI using a commercial gadolinium agent, Gd(HP-DO3A), also revealed no significant difference in the K^{trans} values, a measure of capillary permeability, of L1210-WT- and L1210–10K tumors (Fig. S6). Additionally, many other factors, including human equilibrative nucleoside transporter 1 (hENT1) (48), mitochondrial thymidine kinase (TK2) (49), and cytidine deaminase (CDA) (50), can affect the amount of dC/dCTP in cells, and consequently the apparent CEST signal. Therefore, caution has to be taken in the interpretation of dC-enhanced CEST MRI results. On the other hand, it makes dC-enhanced CEST MRI versatile because it can be potentially used to detect the combination of these factors. Regardless, dC/dCTP accumulation can be considered as an overall biomarker for effective drug accumulation in the tumor cells and thereby as a predictor for tumor responses. Our results confirm the correlation between the tumor resistance to gemcitabine and their low CEST contrast enhancement after dC injection. Further preclinical and clinical testing, however, is required to fully characterize the sensitivity and specificity of dC-enhanced CEST MRI to predict the tumor response to nucleotide-based chemotherapies, for instance those using dFdC and ara-C. For example, DCK activity should be monitored longitudinally in the course of gemcitabine treatment using both non-invasive CEST MRI and invasive methods such as Western Blot or immunohistochemistry so as to validate the utility of our method in measuring the acquired chemoresistance.

In summary, we developed a new “natural” MRI approach for detecting DCK enzymatic activity, in which its natural substrate dC was directly used as an MRI contrast agent to generate CEST signal enhancement in DCK(+) tumors cells without any additional chemical

labeling. We successfully demonstrated this approach in a mouse leukemia model implanted with both DCK(+) and DCK(−) tumors, confirming its ability to detect DCK activity and to predict the tumor response to chemotherapy. Using natural and currently approved drug analogs as MRI contrast agents has great potential to safely stratify patients for the appropriate treatment.

Supplementary Material

Refer to Web version on PubMed Central for supplementary material.

Additional information:

Supported by NIH grants R03EB021573, R01CA211087 and R21CA215860. We sincerely thank Dr. Caius Radu at UCLA for his help with cells and antibodies. Dr. Guanshu Liu devised the research. Drs. Zheng Han, Guanshu Liu, Jia Zhang, Jing Liu and Yuguo Li performed MRI experiments and data analyses. Drs. Zheng Han, Peter van Zijl, and Guanshu Liu drafted the manuscript.

References and Notes:

1. Jordheim LP, Dumontet C. Review of recent studies on resistance to cytotoxic deoxynucleoside analogues. Biochim Biophys Acta. 2007;1776:138–59. [PubMed: 17881132]
2. Sebastiani V, Ricci F, Rubio-Viqueira B, Kulesza P, Yeo CJ, Hidalgo M, et al. Immunohistochemical and genetic evaluation of deoxycytidine kinase in pancreatic cancer: relationship to molecular mechanisms of gemcitabine resistance and survival. Clin Cancer Res. 2006;12:2492–7. [PubMed: 16638857]
3. Bergman AM, Pinedo HM, Peters GJ. Determinants of resistance to 2',2'-difluorodeoxycytidine (gemcitabine). Drug Resist Updat. 2002;5:19–33. [PubMed: 12127861]
4. Huang P, Chubb S, Hertel LW, Grindey GB, Plunkett W. Action of 2',2'-difluorodeoxycytidine on DNA synthesis. Cancer Res. 1991;51:6110–7. [PubMed: 1718594]
5. Kroep JR, Loves WJ, van der Wilt CL, Alvarez E, Talianidis I, Boven E, et al. Pretreatment deoxycytidine kinase levels predict in vivo gemcitabine sensitivity. Mol Cancer Ther. 2002;1:371–6. [PubMed: 12477049]
6. Sigmond J, Kroep JR, Loves W, Codacci-Pisanelli G, Peters GJ. Quantitative real time PCR of deoxycytidine kinase mRNA by Light Cycler PCR in relation to enzyme activity and gemcitabine sensitivity. Cancer Lett. 2004;213:173–9. [PubMed: 15327832]
7. Laing RE, Walter MA, Campbell DO, Herschman HR, Satyamurthy N, Phelps ME, et al. Noninvasive prediction of tumor responses to gemcitabine using positron emission tomography. Proc Natl Acad Sci U S A. 2009;106:2847–52. [PubMed: 19196993]
8. Antonios JP, Soto H, Everson RG, Moughon DL, Wang AC, Orpilla J, et al. Detection of immune responses after immunotherapy in glioblastoma using PET and MRI. Proc Natl Acad Sci U S A. 2017;114:10220–5. [PubMed: 28874539]
9. Koretsky AP, Brosnan MJ, Chen LH, Chen JD, Van Dyke T. NMR detection of creatine kinase expressed in liver of transgenic mice: determination of free ADP levels. Proc Natl Acad Sci U S A. 1990;87:3112–6. [PubMed: 2326269]
10. Walter G, Barton ER, Sweeney HL. Noninvasive measurement of gene expression in skeletal muscle. Proc Natl Acad Sci U S A. 2000;97:5151–5. [PubMed: 10805778]
11. Shapiro MG, Szablowski JO, Langer R, Jasanoff A. Protein nanoparticles engineered to sense kinase activity in MRI. J Am Chem Soc. 2009;131:2484–6. [PubMed: 19199639]
12. Airan RD, Bar-Shir A, Liu G, Pelled G, McMahon MT, van Zijl PC, et al. MRI biosensor for protein kinase A encoded by a single synthetic gene. Magn Reson Med. 2012;68:1919–23. [PubMed: 23023588]

13. Bar-Shir A, Liu G, Liang Y, Yadav NN, McMahon MT, Walczak P, et al. Transforming thymidine into a magnetic resonance imaging probe for monitoring gene expression. J Am Chem Soc. 2013;135:1617–24. [PubMed: 23289583]
14. Pierre VC, Allen MJ, Caravan P. Contrast agents for MRI: 30+ years and where are we going? J Biol Inorg Chem. 2014;19:127–31. [PubMed: 24414380]
15. Chan KW, McMahon MT, Kato Y, Liu G, Bulte JW, Bhujwalla ZM, et al. Natural D-glucose as a biodegradable MRI contrast agent for detecting cancer. Magn Reson Med. 2012;68:1764–73. [PubMed: 23074027]
16. Walker-Samuel S, Ramasawmy R, Torrealdea F, Rega M, Rajkumar V, Johnson SP, et al. In vivo imaging of glucose uptake and metabolism in tumors. Nat Med. 2013;19:1067–72. [PubMed: 23832090]
17. Liu G, Moake M, Har-el YE, Long CM, Chan KW, Cardona A, et al. In vivo multicolor molecular MR imaging using diamagnetic chemical exchange saturation transfer liposomes. Magn Reson Med. 2012;67:1106–13. [PubMed: 22392814]
18. Li Y, Chen H, Xu J, Yadav NN, Chan KW, Luo L, et al. CEST theranostics: label-free MR imaging of anticancer drugs. Oncotarget. 2016;7:6369–78. [PubMed: 26837220]
19. Liu H, Jablonska A, Li Y, Cao S, Liu D, Chen H, et al. Label-free CEST MRI detection of citicoline-liposome drug delivery in ischemic stroke. Theranostics. 2016;6:1588–600. [PubMed: 27446492]
20. Liu G, Song X, Chan KW, McMahon MT. Nuts and bolts of chemical exchange saturation transfer MRI. NMR Biomed. 2013;26:810–28. [PubMed: 23303716]
21. Liu G, Liang Y, Bar-Shir A, Chan KW, Galpoththawela CS, Bernard SM, et al. Monitoring enzyme activity using a diamagnetic chemical exchange saturation transfer magnetic resonance imaging contrast agent. J Am Chem Soc. 2011;133:16326–9. [PubMed: 21919523]
22. Jordheim LP, Cros E, Gouy MH, Galmarini CM, Peyrottes S, Mackey J, et al. Characterization of a gemcitabine-resistant murine leukemic cell line: Reversion of in vitro resistance by a mononucleotide prodrug. Clin Cancer Res. 2004;10:5614–21. [PubMed: 15328204]
23. Barnett BP, Arepally A, Stuber M, Arifin DR, Kraitchman DL, Bulte JW. Synthesis of magnetic resonance-, X-ray- and ultrasound-visible alginate microcapsules for immunoisolation and noninvasive imaging of cellular therapeutics. Nat Protoc. 2011;6:1142–51. [PubMed: 21799484]
24. Chan KW, Liu G, Song X, Kim H, Yu T, Arifin DR, et al. MRI-detectable pH nanosensors incorporated into hydrogels for in vivo sensing of transplanted-cell viability. Nat Mater. 2013;12:268–75. [PubMed: 23353626]
25. Le Belle JE, Harris NG, Williams SR, Bhakoo KK. A comparison of cell and tissue extraction techniques using high-resolution 1H-NMR spectroscopy. NMR Biomed. 2002;15:37–44. [PubMed: 11840551]
26. Beckonert O, Keun HC, Ebbels TM, Bundy J, Holmes E, Lindon JC, et al. Metabolic profiling, metabolomic and metabonomic procedures for NMR spectroscopy of urine, plasma, serum and tissue extracts. Nat Protoc. 2007;2:2692–703. [PubMed: 18007604]
27. Mehrara E, Forssell-Aronsson E, Ahlman H, Bernhardt P. Specific growth rate versus doubling time for quantitative characterization of tumor growth rate. Cancer Res. 2007;67:3970–5. [PubMed: 17440113]
28. Ryoo D, Xu X, Li Y, Tang JA, Zhang J, van Zijl PCM, et al. Detection and quantification of hydrogen peroxide in aqueous solutions using chemical exchange saturation transfer. Anal Chem. 2017;89:7758–64. [PubMed: 28627877]
29. Alic L, van Vliet M, van Dijke CF, Eggermont AM, Veenland JF, Niessen WJ. Heterogeneity in DCE-MRI parametric maps: a biomarker for treatment response? Phys Med Biol. 2011;56:1601–16. [PubMed: 21335648]
30. Zaiss M, Xu J, Goerke S, Khan IS, Singer RJ, Gore JC, et al. Inverse Z-spectrum analysis for spillover-, MT-, and T1 -corrected steady-state pulsed CEST-MRI--application to pH-weighted MRI of acute stroke. NMR Biomed. 2014;27:240–52. [PubMed: 24395553]
31. Bunimovich YL, Nair-Gill E, Riedinger M, McCracken MN, Cheng D, McLaughlin J, et al. Deoxycytidine kinase augments ATM-Mediated DNA repair and contributes to radiation resistance. PLoS One. 2014;9:e104125. [PubMed: 25101980]

32. Arifin DR, Long CM, Gilad AA, Alric C, Roux S, Tillement O, et al. Trimodal gadolinium-gold microcapsules containing pancreatic islet cells restore normoglycemia in diabetic mice and can be tracked by using US, CT, and positive-contrast MR imaging. Radiology. 2011;260:790–8. [PubMed: 21734156]
33. Xu X, Yadav NN, Knutsson L, Hua J, Kalyani R, Hall E, et al. Dynamic glucose-enhanced (DGE) MRI: Translation to human scanning and first results in glioma patients. Tomography. 2015;1:105–14. [PubMed: 26779568]
34. Shi C, Liu D, Xiao Z, Zhang D, Liu G, Liu G, et al. Monitoring tumor response to anti-vascular therapy using non-contrast intravoxel incoherent motion diffusion-weighted MRI. Cancer Research. 2017:canres. 2499.016.
35. Hubeek I, Peters GJ, Broekhuizen AJ, Talianidis I, Sigmond J, Gibson BE, et al. Immunocytochemical detection of deoxycytidine kinase in haematological malignancies and solid tumours. J Clin Pathol. 2005;58:695–9. [PubMed: 15976334]
36. Dekkers IA, Roos R, van der Molen AJ. Gadolinium retention after administration of contrast agents based on linear chelators and the recommendations of the European Medicines Agency. Eur Radiol. 2018;28:1579–84. [PubMed: 29063255]
37. Kang KM, Choi SH, Hwang M, Yun TJ, Kim JH, Sohn CH. T1 shortening in the globus pallidus after multiple administrations of gadobutrol: Assessment with a multidynamic multiecho sequence. Radiology. 2018;287:258–66. [PubMed: 29091750]
38. Liu G, Ray Banerjee S, Yang X, Yadav N, Lisok A, Jablonska A, et al. A dextran-based probe for the targeted magnetic resonance imaging of tumours expressing prostate-specific membrane antigen. Nat Biomed Eng. 2017;1:977–82. [PubMed: 29456877]
39. Presant CA, Wolf W, Albright MJ, Servis KL, Ring R 3rd, Atkinson D, et al. Human tumor fluorouracil trapping: clinical correlations of in vivo 19F nuclear magnetic resonance spectroscopy pharmacokinetics. J Clin Oncol. 1990;8:1868–73. [PubMed: 2230874]
40. Rivlin M, Navon G. CEST MRI of 3-O-methyl-D-glucose on different breast cancer models. Magn Reson Med. 2018;79:1061–9. [PubMed: 28497566]
41. Reagan-Shaw S, Nihal M, Ahmad N. Dose translation from animal to human studies revisited. FASEB J 2008;22:659–61. [PubMed: 17942826]
42. Tiefenthaler M, Hohla F, Strasser-Wozak E, Bacher N, Muhlmann O, Wein W, et al. Delayed addition of deoxycytidine protects normal CD34+ cells against cytotoxicity of gemcitabine without compromising its activity against human leukemic cells. Stem Cells. 2003;21:266–71. [PubMed: 12743321]
43. Bhalla K, Birkhofer M, Li G, Grant S, MacLaughlin W, Cole J, et al. 29-Deoxycytidine protects normal human bone marrow progenitor cells in vitro against the cytotoxicity of 39-azido-39-deoxythymidine with preservation of antiretroviral activity. Blood. 1989;74:1923–8. [PubMed: 2572282]
44. Fox RM, Tripp EH, Tattersall MH. Mechanism of deoxycytidine rescue of thymidine toxicity in human T-leukemic lymphocytes. Cancer Res. 1980;40:1718–21. [PubMed: 6989492]
45. Penit C, Papiernik M. Regulation of thymocyte proliferation and survival by deoxynucleosides. Deoxycytidine produced by thymic accessory cells protects thymocytes from deoxyguanosine toxicity and stimulates their spontaneous proliferation. Eur J Immunol. 1986;16:257–63. [PubMed: 3514238]
46. Peters GJ, Clavel M, Noordhuis P, Geyssen GJ, Laan AC, Guastalla J, et al. Clinical phase I and pharmacology study of gemcitabine (2', 2'-difluorodeoxycytidine) administered in a two-weekly schedule. J Chemother. 2007;19:212–21. [PubMed: 17434832]
47. Blanchard OL, Smoliga JM. Translating dosages from animal models to human clinical trials--revisiting body surface area scaling. FASEB J. 2015;29:1629–34. [PubMed: 25657112]
48. Spratlin J, Sangha R, Glubrecht D, Dabbagh L, Young JD, Dumontet C, et al. The absence of human equilibrative nucleoside transporter 1 is associated with reduced survival in patients with gemcitabine-treated pancreas adenocarcinoma. Clin Cancer Res. 2004;10:6956–61. [PubMed: 15501974]
49. Eriksson S, Kierdaszuk B, Munchpetersen B, Oberg B, Johansson NG. Comparison of the substrate specificities of human thymidine kinase-1 and kinase-2 and deoxycytidine kinase toward antiviral

and cytostatic nucleoside analogs. Biochemical and Biophysical Research Communications. 1991;176:586–92. [PubMed: 2025274]

50. Eda H, Ura M, FO K, Tanaka Y, Miwa M, Ishitsuka H. The antiproliferative activity of DMDC is modulated by inhibition of cytidine deaminase. Cancer Res. 1998;58:1165–9. [PubMed: 9515801]

Significance

A new molecular MRI method that detects deoxycytidine kinase activity using its natural substrate deoxycytidine has great translational potential for clinical assessment of tumor resistance and prediction of treatment efficacy.

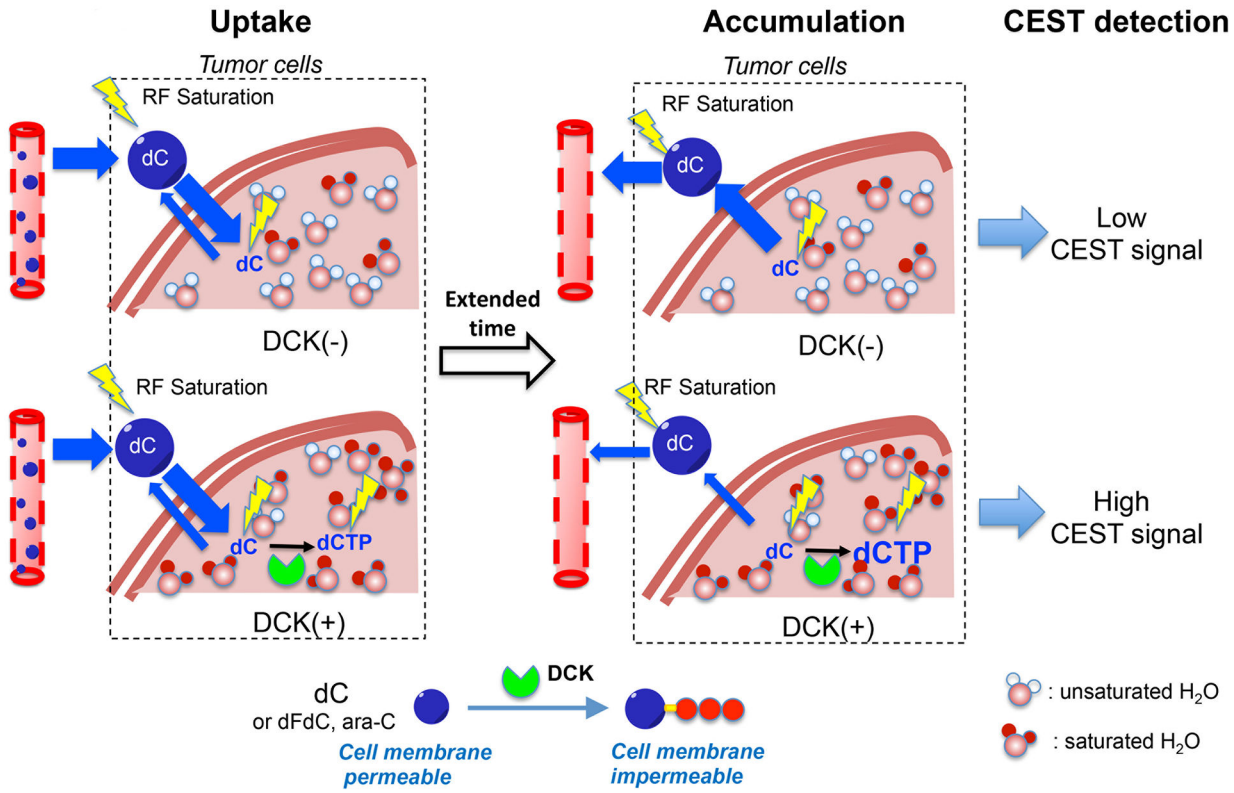

Fig. 1. Schematic illustration of CEST MRI detection of DCK activity using natural dC as the contrast agent.

dC and dCTP have different cell permeability- dC can diffuse across cell membrane freely, whereas dCTP cannot. In DCK(−) cells, the intracellular dC concentration will increase first as a result of the initial spike of the intravascular dC concentration after the systemic injection, followed by a quick decrease due to the efflux of dC from cells. Conversely, in DCK(+) cells, the influxed dC is phosphorylated to dCMP, which will be spontaneously converted to dCTP in the cells, leading to the accumulation of dCTP intracellularly. Because both dC and dCTP can be detected by CEST MRI by their amine protons, the intracellularly accumulated dCTP will result in an elevated CEST signal. Hence, one can use the increase of CEST signal at an extended time point after the injection of dC to quantify dCK activity and distinguish DCK(−) and DCK(+) tumor cells

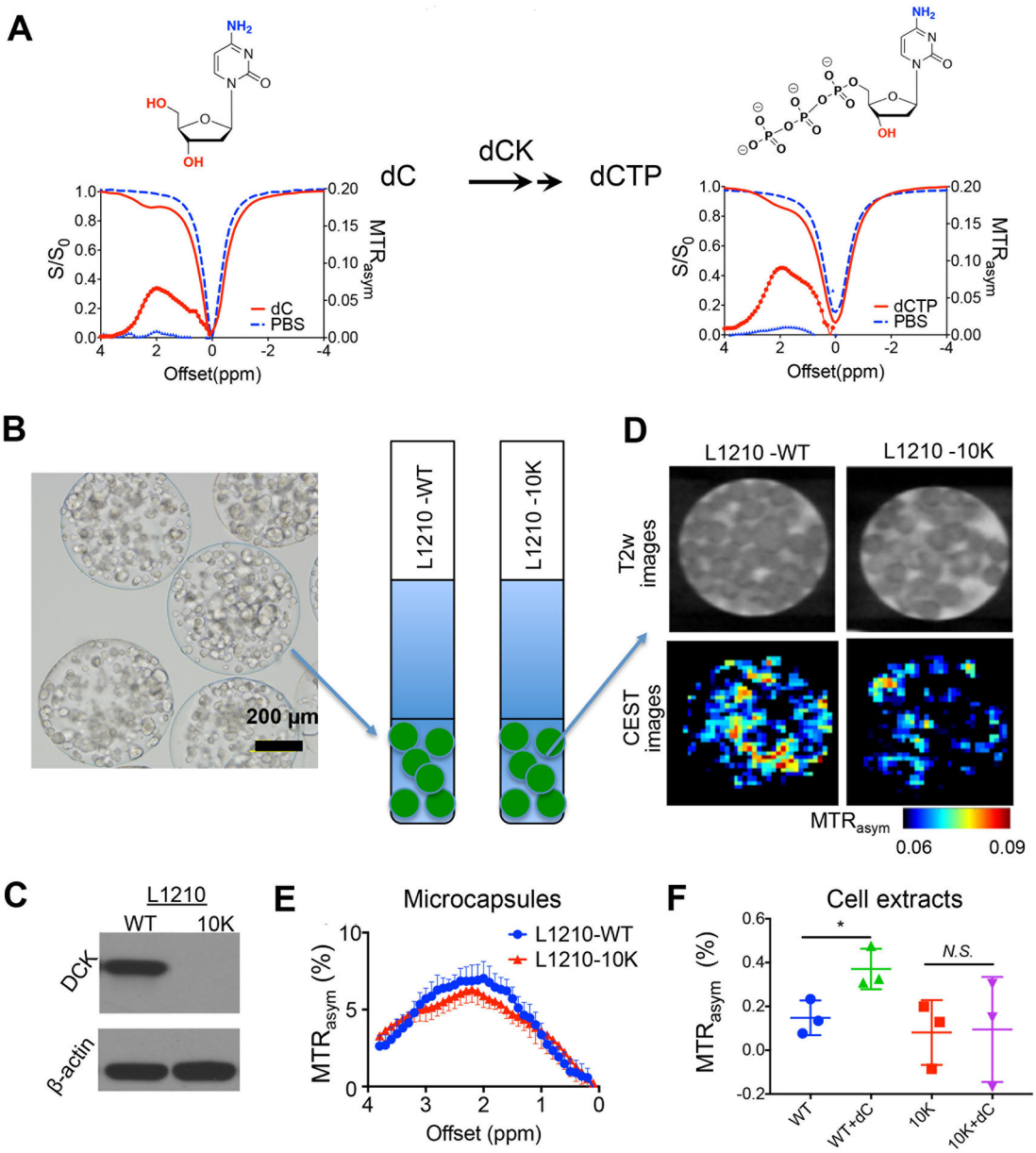

Fig. 2. ***In vitro*** **CEST MRI detection of DCK activity.**

(A) Chemical structures and CEST signal (Z-spectra (S/S_0) and MTR_{asym} plots) of the substrate (dC) and final product (dCTP) of dCK reaction, respectively. All solutions were 10 mM (pH 7.4 and 37 °C) in PBS. (B) A representative light microscopic image of microcapsule-encapsulated cells (left), which were imaged in PBS buffer in 5 mm NMR tubes (right). (C) Western blot confirming the different DCK expression levels in L1210-WT and L1210–10K cells. β-actin was used as loading control. (D) T_2-weighted (T_2w) images and corresponding CEST images of microcapsule-encapsulated DCK(+) L1210-WT and DCK(−) L1210–10K after incubating in cell culture medium containing 5 mM dC for 12 hours after washing three times using PBS. (E) Comparison of the MTR_{asym} plots of the two types of cells in microcapsules after dC incubation. Error bars are the standard deviations of

the measurements. (F) MTR_{asym} at 2 ppm of cell extracts of 1×10^7 L1210-WT and L1210–10K cells (diluted to 50 μL in PBS pH 7.4), with or without dC incubation for 24h. *, $p<0.05$, n=3.

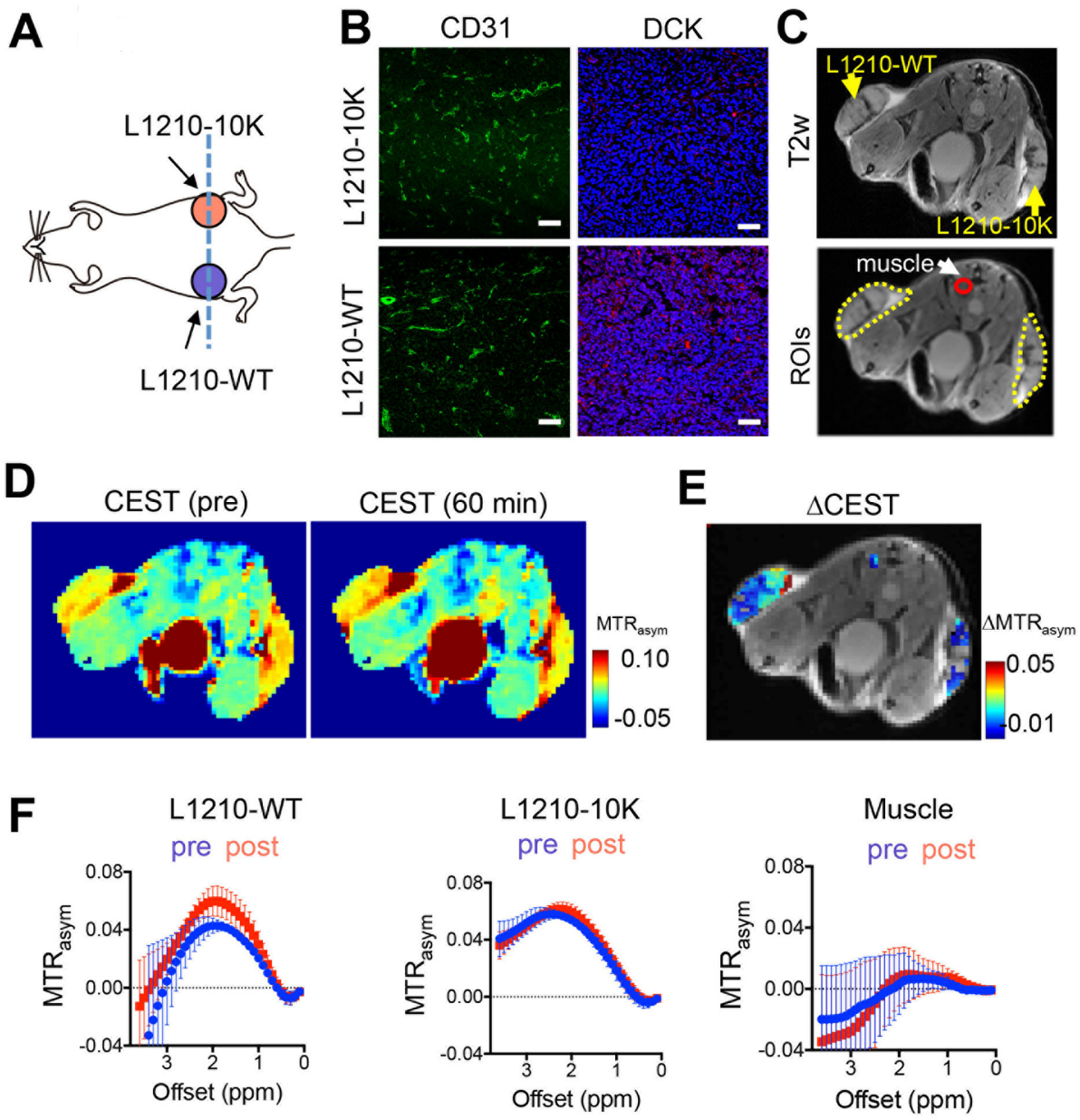

Fig. 3. *In vivo* CEST MRI detection of DCK activity in tumors with different DCK activity in a representative mouse.

(A) Illustration of tumor inoculation position and imaging plane (blue dashed line). **(**B) Fluorescence images of CD31 and DCK staining of the L1210-WT and L1210–10K tumors, respectively. Green: CD31; Red: DCK; Blue: DAPI. Scale bar: 50 μm. (C) T_2w image showing the locations of DCK (+) L1210-WT (left flank) and DCK(−) L1210–10K tumors (right flank) and an image showing three ROIs encompassing the two tumors and muscle. (D) Representative MTR_{asym} maps at 2.0 ppm before and 60 minutes after the injection. (E) Overlay image showing the CEST contrast enhancement (ΔMTR_{asym}) in the two tumors at 60 minutes post-injection. ΔMTR_{asym} is defined by $MTR_{asym}(t)$-MTR_{asym}(pre). (F) Mean ROI CEST signal (MTR_{asym} plots) of pre- and 60 minutes post-injection (n=4).

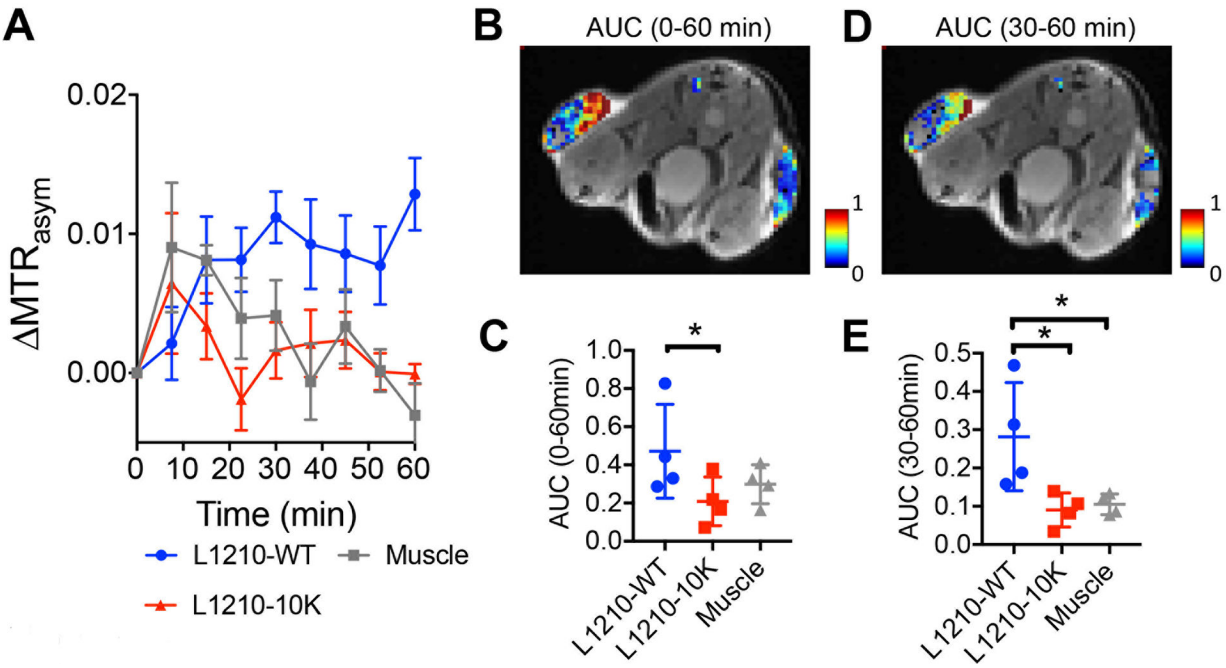

Fig. 4. Dynamic CEST MRI contrast in tumors with different DCK activity.

(A) Dynamic changes for the mean ΔMTR_{asym} (2ppm) in the two tumors and muscle. Data are presented as mean±SEM of all the pixels within each ROI (n=4). (B) Overlay image showing the AUC (area under the curve) of the three regions over the period 0 to 60 minutes post-injection. (C) Comparison of the mean AUC (0–60 min) between DCK(+) tumors and DCK(−) tumors (n=4; two-tailed Student's t-test, *: $p<0.05$). (D) Overlay image showing the AUC (area under the curve) of the three regions over the period 30 to 60 minutes post-injection. (E) Comparison of the mean AUC (30 −60 min) between DCK (+) tumors and DCK (−) tumors (n=4; two-tailed Student's t-test, *:$p<0.05$).

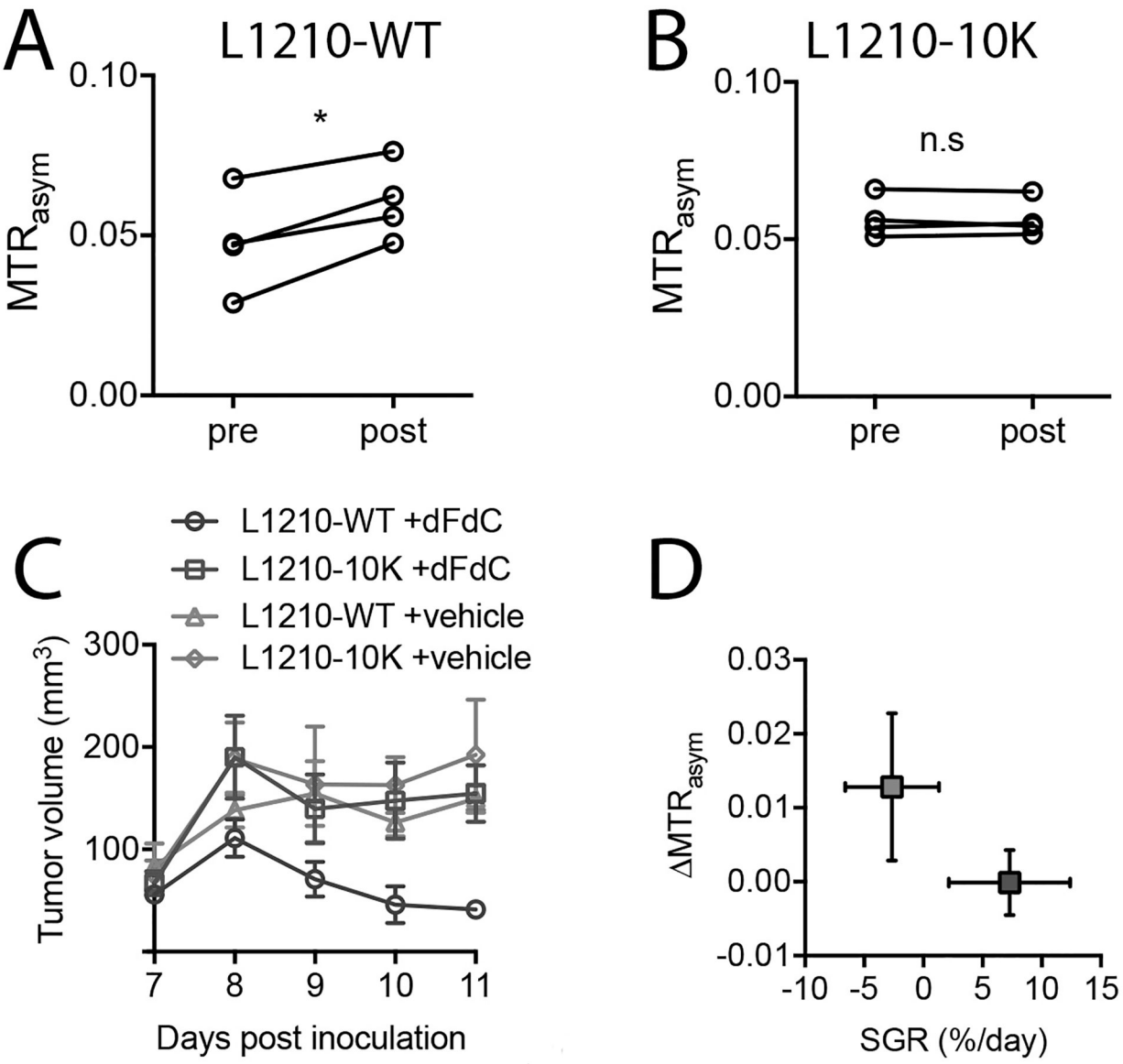

Fig.5. Using dC-enhanced CEST MRI to stratify tumors with different DCK activity and to predict tumor response to gemcitabine.

Scatter plots of MTR_{asym} values of four L1210-WT before (pre) and at 60 min after (post) injection of dC (A) and four L1210–10K (B) tumors. *: $p<0.05$. n.s.: not significant (two-tailed paired Student's t-test, n=4). (C) Treatment response to gemcitabine in L1210-WT and L1210–10K tumors as quantified by the tumor growth. Treatment (a single dose of 360 mg/kg dFdC, *i.p.*) was carried out at day 7 after tumor inoculation (n=5 per group). (D) Correlation between the mean CEST (ΔMTR_{asym}) and specific growth rate $\ln(volume^{day11}/volume^{day7})/5\times 100\%$ for L1210-WT and L1210–10K tumors respectively. Errors are the standard deviations of the measured ΔMTR_{asym} (n=4) and tumor growth rate (n=5) among tumors. Red box: L1210-WT; blue box: L1210–10K.